Chemical Engineering & Processing: Process Intensification 153 (2020) 107924

Contents lists available at ScienceDirect

Chemical Engineering & Processing: Process Intensification

journal homepage: www.elsevier.com/locate/cep

Deep data analysis for aspiration pressure estimation in a high-pressure gas atomization process using an artificial neural network

Rashed Kaiser, Songkil Kim*, Donggeun Lee*

School of Mechanical Engineering, Pusan National University, Busan 46241, Republic of Korea

ARTICLE INFO

Keywords:
Gas atomization
Artificial neural network
Aspiration pressure
Nozzle design
Nozzle operation

ABSTRACT

This study was devoted to introducing a new method for a priori prediction of aspiration pressure buildup in closed coupled atomization (CCA) nozzles. There have been considerable controversies about increasing or decreasing the aspiration pressure for a reliable operation of CCA nozzles, mainly because of the complex nature of CCA process. Here for the first time, we applied an artificial neural network (ANN) based machine learning algorithm for the prediction of aspiration pressure in close-coupled HPGA nozzles. An analytical model equation was obtained based on the largest experimental dataset from the literature and proved to be useful for prediction of non-dimensionalized aspiration pressure with R^2 of 0.98. But, its prediction accuracy of absolute aspiration pressures was degraded with a decrease of R^2 score to 0.73 and an average prediction error of 17 %, mainly due to the limitation of literature data. Based on parametric study and a sensitivity test, protrusion length of CCA nozzles and Re number were found to be relatively significant as compared to the apex angles. Finally, we provided a comprehensive contour map to facilitate the conceptual design and operation of CCA nozzles to minimize the aspiration pressure.

1. Introduction

Close-coupled atomization (CCA) of a molten metal is the preferred choice for producing fine powders (< 20 μm) and provides improved efficiency in the powder manufacturing industries [1]. The atomization process requires a high level of gas-to-melt momentum transfer to strengthen primary and secondary breakup of the melt before the melt droplets are solidified [2,3]. Hence, a large number of previous studies have concentrated on elucidating the mutual interaction of supersonic gas streams and droplets of metal melt, when altering the design and operation parameters of nozzles. These parameters include such as the protrusion length and apex angle of a melt feeding tube, as well as injection pressure and physical properties of the gas, and the gas-to-melt ratio (GMR) [4–17]. In fact, many of the previous studies have been driven toward producing smaller metal powder by developing their own designs of CCA nozzles, but modern CCA technology seems to have reached a limit for producing sub-10 μm powder and to face a new practical challenge of stable operation of the nozzles as well.

In our opinion, an aspiration pressure, that is developed at the melt-tube tip of CCA nozzles by the back flow of gas, lies in the middle of the stable operation issue. There has been considerable discussion of the possible roles of aspiration pressure in the size of metal powder and the stability issue of CCA process. Increasing the aspiration pressure above the ambient pressure reduces the melt flow rate so that increases the GMR, and at the same time it can push the melt to form a sheet at the edge of melt tube, activating the popular melt sheet mode [18]. Although these actions of aspiration pressure are all beneficial for reducing the powder size, a high aspiration pressure is not always recommended. When aspiration pressure sometimes becomes unexpectedly large or fluctuated by any means, it can directly impede the flow of melt through the tube, or cause intermittent pause of the flow, which results in freezing of the melt inside the melt tube. Another concern is that a high positive (over-ambient) aspiration pressure, if not precisely controlled, can push the melt sheet further beyond the edge, which might lead to an early gas flow separation [9,10,18,21,19] and lick back phenomena [21,19] of melt on the outer wall of the melt tube.

Conversely, when it comes to lowering the aspiration pressure, a negative (sub-ambient) aspiration pressure may create a suction around the melt tube tip that will help to make the melt flow smooth and attract the mainstream of gas on to the outer wall of melt tube to minimize the gas separation as well [4,12,15,21,19]. Since such a low aspiration pressure seems to be more advantageous at least for the stability issue of CCA nozzles, we would like to introduce our methodology and outcomes toward that direction from now on.

The problem is that the aspiration pressure is not easy to predict until the nozzle design is determined. This is because the aspiration

---

* Corresponding authors.
E-mail addresses: songkil.kim@pusan.ac.kr (S. Kim), donglee@pusan.ac.kr (D. Lee).

https://doi.org/10.1016/j.cep.2020.107924
Received 12 September 2019; Received in revised form 8 March 2020; Accepted 11 April 2020

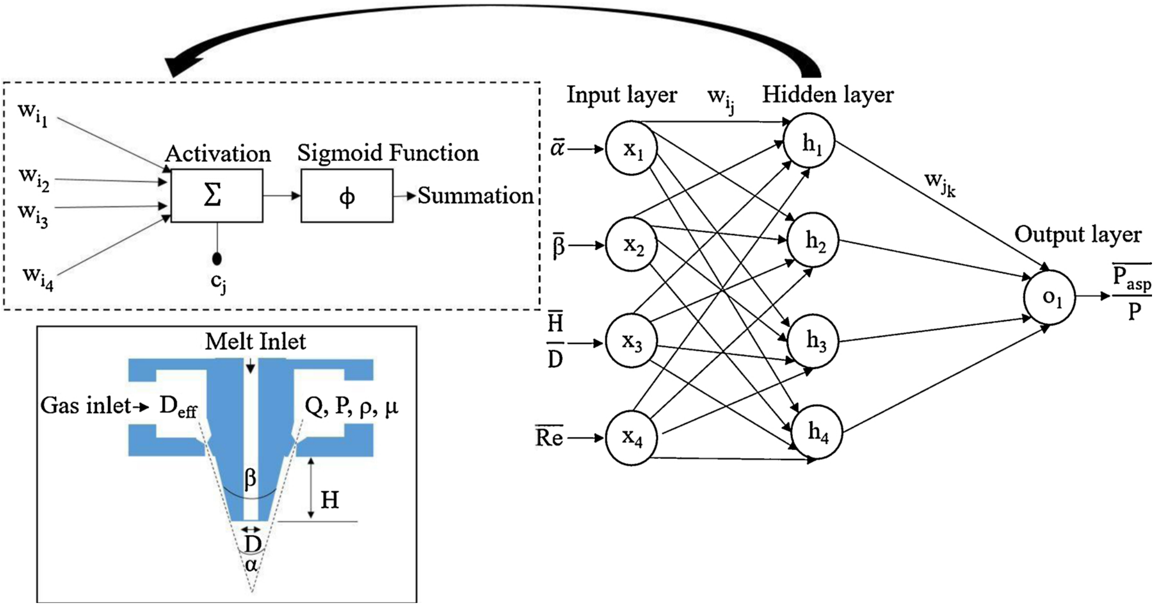

Fig. 1. Schematic of the artificial neural network (ANN) utilized in the present study with detailed illustrations of the function of the hidden layers and, of the gas flow and nozzle design parameters.

pressure is created in response to supersonic flow fields, which means that all the aforementioned parameters are involved in determination of the pressure. Moreover, it is not possible to measure the aspiration pressure in reality in which metal melt is injecting into the gas through its delivery tube. [10] In fact, all the literature data of aspiration pressure were obtained in the absence of melt flow. Upon injection of melt, the real gas pressure at the center of melt tube tip might be considerably different from the aspiration pressure [1]. As such, despite those existing controversies and limitations, understanding the aspiration pressure buildup in connection with wake structures has long been an attractive subject of researches.

Ting et al. [1] observed a sudden change of aspiration pressure when the gas-injection pressure (*P*) varied around a critical value, known as “the wake-closure pressure” (WCP), particularly from convergent-type of CCA nozzles. When $P <$ WCP, the recirculation (wake) zone is shaped like an hour-glass of which the downstream end is open. Thus, this type of recirculation zone is called “open wake”. When *P* increases and approximates the WCP, the stronger gas stream impacts the melt flow so that it squeezes the neck of the hour-glass wake more. When *P* slightly exceeds the WCP, the neck is apparently cut off and the wake appears closed with a sharp end.

Compared to the open-wake condition, the recirculation zone becomes shortened in length and its strength noticeably weakened under this closed-wake condition ($P >$ WCP) [1,18,19,20]. This leads to a sudden reduction of the aspiration pressure to less than the ambient pressure in response to the mass change of gas entering the recirculation zone [1,19,20]. On the other hand, holding the injection pressure (*P*) high is not always recommended because it can create a strong Mach disk at the truncated end of the wake zone, followed by a series of shock waves. This is detrimental to effective gas-momentum transfer to the melt. It is therefore important to determine the range of allowable gas injection (or aspiration) pressures relevant to particular nozzle configurations. In contrast to the convergent CCA nozzles [13,19,20], convergent-divergent (C–D) CCA nozzles [9,10,16] help the gas to be fully expanded through the nozzle, so that such a Mach disk is not typically observed.

Ridder et al. [20,21] reported that the aspiration pressure first rises to a peak and then falls while the injection pressure steadily increases. Such a volcano-shaped response of the aspiration pressure was similarly observed regardless of gas types (i.e., with He, N_2, and Ar) although there was a slight difference in degree. Moreover, much experimental works [9,10,12,13,16] suggested that high injection pressures of gas used to be helpful to reduce the aspiration pressure below the ambient pressure, whereas at relatively low pressures, a longer protrusion length of the melt tube sometimes create a positive (over-ambient) peak of aspiration pressure for both types of CCA nozzles. Cui et al. [4] and Zhao et al. [16] found that the aspiration pressure increases with increase of the apex angle of an C–D CCA nozzle.

Despite the large number of previous studies, there is no analytical model capable of a priori prediction of the aspiration pressure directly from the design parameters and process parameters. The reason might be the fact that there are too many factors involved to derive a single model equation. In order to circumvent this technical challenge, we first used Buckingham’s Π theorem [22] to reduce the number of parameters of interest and then applied a machine learning approach using an artificial neural network (ANN) with experimental datasets from the literature. As a result, an analytical model equation was obtained and further validated with an extra dataset. Sensitivity analysis was also conducted to extract two most significant (dimensionlesss) parameters affecting the aspiration pressure, which result was also supported with a comprehensive computational fluid dynamic (CFD) analysis. Based on these results, we finally proposed a contour map relating the aspiration pressure to the significant parameters.

2. Theory and methodology

2.1. Non-dimensionalized functional relation between aspiration pressure and systematic parameters

Aspiration pressure (P_{asp}) is affected by various process parameters such as injection pressure (*P*), mass flow rate (*Q*), density (ρ), and viscosity (μ) of gas, as well as by nozzle design parameters such as protrusion length (*H*), melt tube diameter (*D*), and the apex angles of jet and nozzle (α and β). [4–17] Most of the parameters are graphically illustrated in the inset of Fig. 1.

The relation can be expressed by

$$P_{asp} = g\,(\alpha,\ \beta,\ H,\ D,\ P,\ Q,\ \rho,\mu) \tag{1}$$

To reduce the number of variables involved in the relation, Buckingham’s Π theorem [22,23] was used to convert Eq. (1) to a

Table 1
Diversity of experimental data used for training ANN.

a) Gas properties

Gas species	Dynamic viscosity μ (kg/m·s)
Argon (Ar)	2.13×10^{-5}
Nitrogen (N_2)	1.72×10^{-5}

b) Process parameters

Injection Pressure P (atm)	Gas Flowrate Q (kg/s)	Reference
16 - 55	0.22 – 0.67*	[13]
9.87 - 34.54	1.3×10^{-2} - 4.3×10^{-2}	[9]
9.96 - 31.58	2.7×10^{-2} - 8.5×10^{-2}	[10]
3.53 - 40.56	5×10^{-4} - 5×10^{-3}**	[16]

c) Nozzle types and design parameters

Nozzle type	Protrusion Length, H (mm)	Jet apex angle α (deg)	Nozzle apex angle β (deg)	Melt tube diameter D (mm)	Reference
Discrete jet Conv.	2.24–12	45	45	10.41–21.34	[13]
Discrete jet C–D	5–15	25	25	3.00	[9]
Annular slit C–D	5	26	46	3.00	[10]
Annular slit C–D	10–14	16–28	22–26	1.20	[16]

* Flow rates were used from similar nozzle and gas study [48].
** Both the throat area and flow rates were used from similar nozzle study [49].

dimensionless form and thereby to simplify the analysis further. We have eight variables with three physical dimensions of mass (M), length (L), and time (T).

Applying the Π theorem to the dimensional variables with three repeating variables of P, D, and ρ, Eq. (1) is now expressed in a dimensionless form with five dimensionless variables (Π_1, Π_2, …, Π_5) as:

$$P_{asp}/P = f(\alpha, \beta, H/D, Re) \tag{2}$$

where P_{asp}/P corresponds to the target variable Π_1, α and β in radians become Π_2 and Π_3, H/D corresponding to Π_4 measures the effect of a protrusion length H, and the last Π_5 represents the Reynolds number defined by $Re = 4Q/(\pi D_{eff} \mu)$. Here, D_{eff} is an area equivalent diameter of the nozzle throat that can be calculated from the area (A) of the nozzle throat by $D_{eff} = (4A/\pi)^{1/2}$. In order to identify the functional form of f in Eq. (2), an artificial neural network (ANN) was applied using a wide range of experimental data collected from the literature [9,10,13,16].

2.2. Basic structure, function, and implementation of an artificial neural network

Fig. 1 shows a schematic of an artificial neural network, which is an interconnected group of nodes called artificial neurons, akin to the vast network of neurons in human brains [24]. Typically, artificial neurons such as those depicted in circles in Fig. 1 are aggregated into three different layers: input, hidden, and output, [25] depending on their tasks. Signals received from external inputs (corresponding to Π_2 - Π_5 in this study) are first stored in the nodes (x_1 to x_4) in the input layer, and then processed to be transmitted to each of the nodes in the hidden layer. These are finally transmitted to an output neuron (corresponding to Π_1) in the output layer. As illustrated in Fig. 1, the four hidden neurons connecting the input neurons and the output neuron play a key function by determining the accuracy of the ANN analysis.

When the four input neurons are designated x_i (indexed with $i = 1$, 2, 3, 4), the four hidden neurons are designated h_j with $j = 1$–4, and the only output neuron is designated o_k with $k = 1$. The connections between the input and hidden layers (depicted with arrows in Fig. 1 and often called "edges") typically have a weight factor (w_{ij}) per pair that is adjusted during the training process to measure the strength of a signal at the connection. In this study, each of the connections between the hidden and output layers are evaluated by w_{jk}.

The boxed inset of Fig. 1 depicts the function of the hidden layer. A neuron in the hidden layer takes a sum of the signals from four input neurons with weights to calculate "activation" as $a_j = \sum_{i=1}^{4} w_{ij}x_i + c_j$ where c_j is a bias. Next, this activation at each hidden neuron is treated using a sigmoid function [26] as $z_j = 2/(1 + \exp(-2a_i)) - 1$, which is then subject to an internal screening with threshold θ_j. Finally, an output signal o_k is calculated through a similar weighted summation as $o_k = \sum_{j=1}^{4} w_{jk}z_j + d_k$ (where d_k is an additional bias) and then is transmitted to the output neuron.

Starting with initialized weights and biases, the Levenberg-Marquardt (LM) backpropagation algorithm is run to calculate a total squared error between the resulting output of the ANN and the target (experimental) output, to iteratively adjust the weights and biases in a gradient-descent direction of the error, and finally to minimize the prediction error [27]. Note that the final set of weights and biases that perform the best for the target dataset used does not necessarily work for other unexperienced datasets. Thus, an ANN being trained likewise is generally crosschecked using two additional processes: validation and test steps [28]. Also note that a large number of data are generally required to prevent "overfitting" of the ANN [29].

With this in mind, we collected two hundred data (206 in total) from four different experiments, [9,10,13,16], which makes it the largest dataset about close-coupled gas atomization nozzles to our knowledge. All the required parameters are provided as a table in Supplementary data. The entire dataset was split into three groups: 80 % for ANN training, 10 % for validation, and 10 % for the final test of the ANN. Data was randomly selected and assigned to each group. The training dataset was used to build multiple algorithms by adjusting different combinations of weights and biases with the training datasets. The validation dataset was used to compare the performance of these prediction algorithms and to choose the algorithm with the best performance. Finally, the test dataset was used to measure the performance of this algorithm [30]. This data assignment and ANN process were repeated until the corresponding outcomes had the minimum error. After confirmation in the test step, the network weights and biases were determined to build the final model equation estimating the output (aspiration pressure) from systematic input parameters. A MATLAB-based code was developed to implement the foregoing ANN analysis for the entire dataset [31]. For reference, details of set-up parameters for running this ANN training are available in Appendix A.

Table 1 describes a diversity of experimental conditions that we considered in terms of nozzle types, gas properties, operation conditions, and nozzle design parameters from the literatures. Based on the experimental conditions, the four input Πs (s = 2, 3, 4, 5) as well as the output Π_1 were calculated as defined in Eq. (2), and some of them are classified into the three different groups for further parametric (sensitivity) studies as listed in Appendix B; where Tables B1 and B2 represent the first and second dataset grouped regarding change of the gas apex angle (α) and nozzle apex angle (β), respectively, while Table B3 shows the third data group combining the dimensionless protrusion length ($\Pi_4 = H/D$) and Re number.

Note that the values of Πs often differ by orders of magnitude in Tables B1–B3 of Appendix B. For example, the values of Re are always one million-times larger in magnitude than other Π variables. This may hinder proper evaluation of each parameter (Π) because the ANN analysis process could be overwhelmed by the largest input parameter [32]. To avoid this problem, all of the input and output Πs were

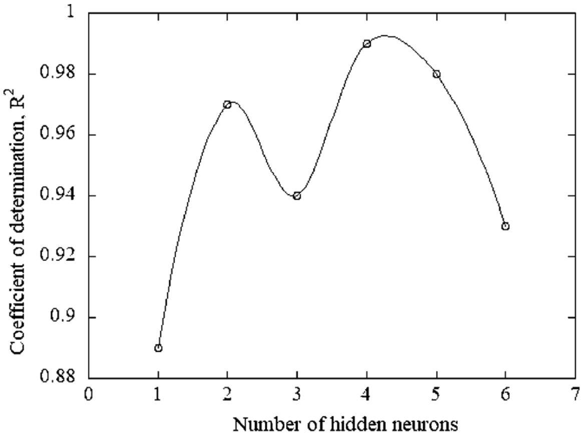

Fig. 2. Variation of coefficient of determination R^2 with the number of hidden neurons.

normalized to vary in the range -1 to 1 by Eq. (3):

$$\bar{x} = 2\,(x - x_{min})/(x_{max} - x_{\min}) - 1 \tag{3}$$

where x = original data, $\bar{x}$ = normalized x, x_{max} = maximum value of x, x_{min} = minimum value of x. This normalization is known to be effective for shortening the learning time and improving the accuracy of the output results as well [33].

According to previous theoretical work [34], a single hidden layer is enough to reasonably approximate any function of the ANN, unless the experimental data under consideration have peculiar discontinuities, such as a sawtooth pattern. Because no discontinuities were found from the present parametric studies, one hidden layer was finally employed. Next, it is of particular interest to select an appropriate number of neurons in the hidden layer, because if too few or too many hidden neurons are selected, this might result in under-fitting or over-fitting of the data, respectively [35–37]. An optimal number of hidden neurons in this study was determined on a trial and error basis, in accordance with the suggestions of previous studies [38,39]. For instance, Fig. 2 shows the variation of R^2 (coefficient of determination) score of ANN predictions with increasing the number of hidden neurons. Starting from a single hidden neuron, the R^2 score increases rapidly, and undergoes a little fluctuation before reaching a maximum of ~0.98 when four hidden neurons used, and then falls with further increase of the number of hidden neurons. Fig. 3 shows likewise the variation of mean squared error (MSE). It is obvious that four hidden neurons are the best choice denoting the highest R^2 score as well as the lowest MSE. More than six hidden neurons are not desirable because it may cause the overfitting of ANN or making the prediction equation complicated in addition to the dissatisfaction with the prediction accuracy. Thus, four neurons were finally employed in this study.

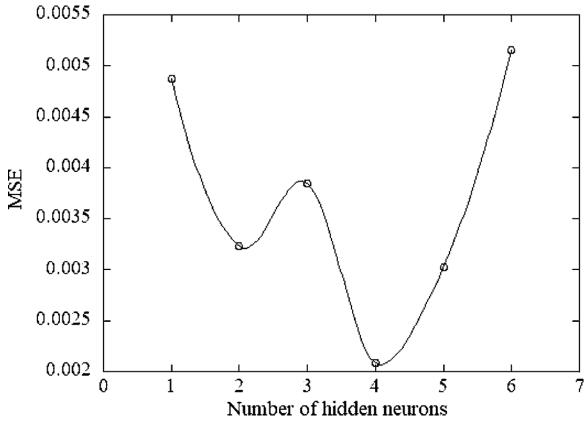

Fig. 3. Variation of MSE (mean squared error) with the number of hidden neurons.

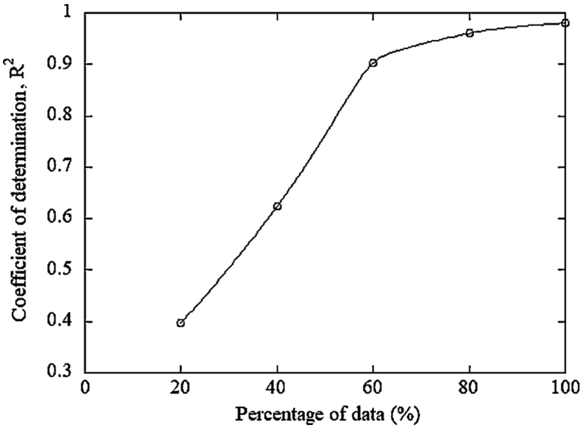

Fig. 4. Variation of coefficient of determination R^2 with the percentage of data.

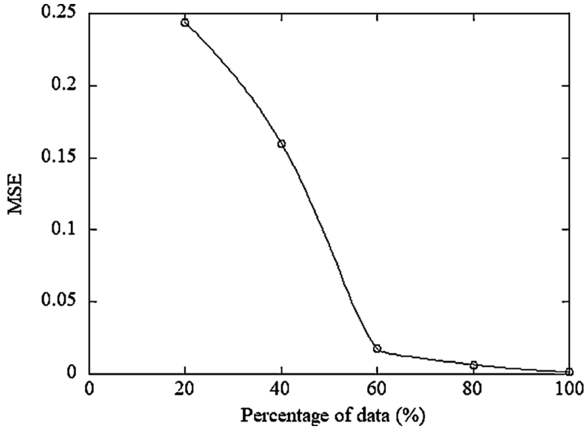

Fig. 5. Variation of MSE (Mean squared error) with the percentage of data.

When it comes to the size of the literature data, another preliminary study was performed similarly. Figs. 4 and 5 show the variations of R^2 score and MSE of ANN predictions with the size of literature data, respectively. The x-axis of the figures denotes what percentage of data has been used to yield the model equation. For instance, 20 % implies that 41 datasets, i.e., 20 % of the 206 (in total) experimental datasets. The 41 datasets has also been randomly divided into three groups such as 80 %, 10 %, and 10 % of the 41 datasets for the subsequent training, validation, and test steps, respectively. This process was repeated while monitoring R^2 score and MSE while increasing the size (percentage) of datasets up to 100 %. Both figures showing opposite trends clearly indicate that 80 % of the 206 datasets are sufficiently large in size ensuring that $R^2 \geq 0.98$ and MSE ≤ 0.005.

2.3. Computational fluid dynamics (CFD) simulation

Computational fluid dynamics simulations (CFD) has also been implemented for understanding features of wake structures in connection with aspiration pressures around wake closure pressure. The CCA nozzle we considered is a convergent nozzle [19] for which a commercial code ANSYS Fluent 16 was used under the assumption of the rotational symmetry of the CCA nozzle. In addition, we considered argon gas flow only without any melt introduction and modelled it as an unsteady compressible flow with Reynolds-stress turbulence model [40]. In order to improve the accuracy and convergence of simulation, a sufficiently small time step of 10^{-5} s was used [41]. Once the steady-state flow field of the gas had been developed, the aspiration pressures were measured by averaging the static pressures along the melt tube tip

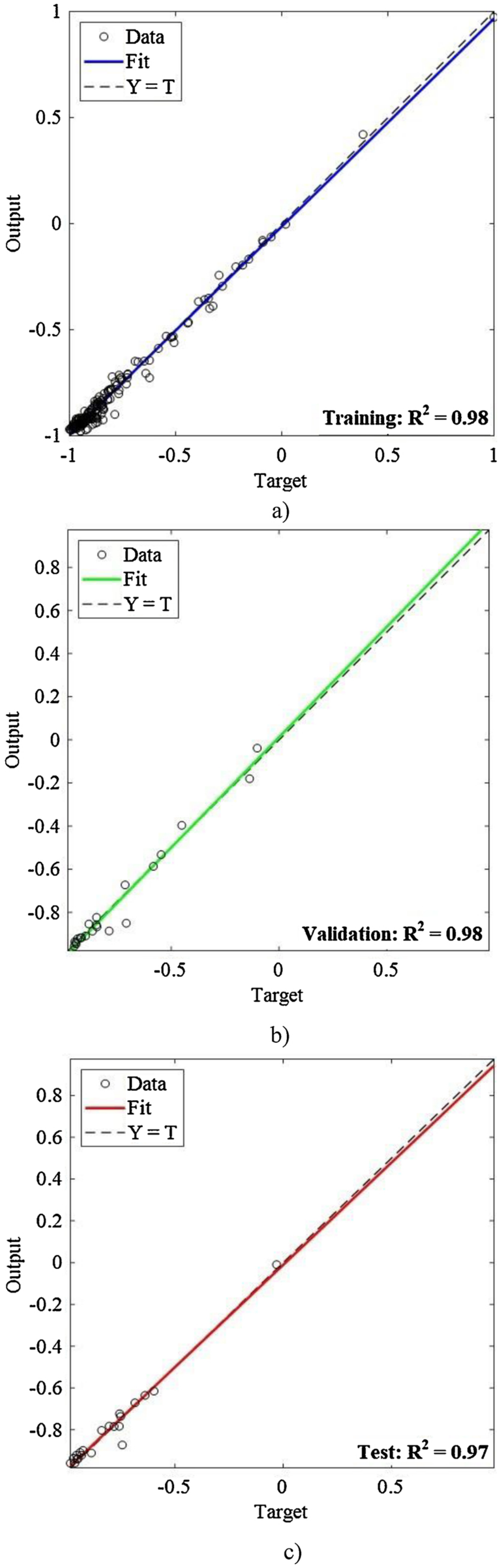

a)

b)

c)

Fig. 6. Regression analysis for the neural network responses: a) Training data, b) Validation data, and c) Test data.

surface as proposed by [19].

3. ANN analysis results and experimental validation

Fig. 6 shows the regression plots of the final outcomes from the three successive steps (training, validation, and testing). In Fig. 6, the solid line representing the best fitting result is almost completely overlapped by the dashed line indicating the perfect prediction (outputs) of the ANN in relation to the experimental data (targets in terms of the normalized P_{asp}/P). Note that the R^2 values in Fig. 6a–c are always higher than 0.97 for the training-to-test steps, suggesting that the present ANN predictions are quite satisfactory, independent of the randomly grouped data. The final model equation used to estimate the aspiration pressure was extracted from the ANN training dataset, written in the non-dimensionalized form in Eq. (4). More details about the preparation, calculation, and post-treatment process of ANN for the equation are available in Appendix C

$$\frac{P_{asp}}{P} = 5.656{-}2.306/(1 + \exp(-2a_1)) + 3.212/(1 + \exp(-2a_2)) - 4.441/(1 + \exp(-2a_3)) - 5.495/(1 + \exp(-2a_4)) \tag{4}$$

Where

$$\begin{aligned} a_1 = {} & (0.253\Pi_2 - 0.137)/0.520 - (0.33\Pi_3 - 0.18)/0.50 \\ & + (0.085\Pi_4 - 0.501)/11.56 + (0.125Re - 2.69 \times 10^6)/4.2 \times 10^7 \\ & - 1.380 \end{aligned}$$

$$\begin{aligned} a_2 = {} & -(0.268\Pi_2 - 0.105)/0.520 + (2.32\Pi_3 - 1.22)/0.50 \\ & + (0.607\Pi_4 - 3.56)/11.56 - (44.960Re - 9.\ .87 \times 10^8)/4.2 \times 10^7 \\ & - 24.237 \end{aligned}$$

$$\begin{aligned} a_3 = {} & (8.429\Pi_2 - 4.56)/0.520 - (0.781\Pi_3 - 0.414)/0.50 \\ & - (1.355\Pi_4 - 7.98)/11.56 + (7.400Re - 1.591 \times 10^8)/4.2 \times 10^7 \\ & + 0.574 \end{aligned}$$

$$\begin{aligned} a_4 = {} & -(6.841\Pi_2 - 3.700)/0.520 - (0.352\Pi_3 - 0.198)/0.50 \\ & - (0.109\Pi_4 - 0.642)/11.56 + (0.031Re - 6.80 \times 10^5)/4.2 \times 10^7 \\ & + 2.607 \end{aligned}$$

It should be noted, here, that Eq. (4) returns only the normalized dimensionless aspiration pressure. Although this model equation seems to work very well for the entire pretreated data, it does not necessarily guarantee that this will fit best the raw (absolute) aspiration pressures. Some unexpected problem can arise from the data handling process. From a mathematical point of view, Eq. (3) is a sort of linear transformation that does not cause any change in the coefficient of determination (R^2). However, taking a close look at the definition of Π_1 (P_{asp}/P), we realized that P_{asp} and P are both case-specific variables so that taking their ratio helps to mitigate their case sensitivities and revealed their universal nature in Fig. 6. Conversely, this implies that the data scatteredness would be more prominent in a graph plotting the raw dimensional data (P_{asp}). Fig. 7 presents ANN predictions of P_{asp} against the corresponding experimental data. As expected, the equation is still reasonably monitoring the P_{asp}, while its prediction accuracy becomes apparently degraded with a decrease of R^2 to 0.73; and an average (relative) prediction error of 17 % (corresponding to MSE of 0.017).

Another reason might be originated from the fact that the dataset involves both types (convergent vs C–D) of CCA nozzles. It is notable that a convergent nozzle and an equivalent C–D nozzle often exhibit different expansion behaviors of gas so that creating a remarkable difference in P_{asp} between them. A simple way to circumvent this issue is to divide the whole dataset into two groups depending on their nozzle types and to obtain a model equation for each. However, we could not, because the size (206) of dataset is not big enough to divide. The

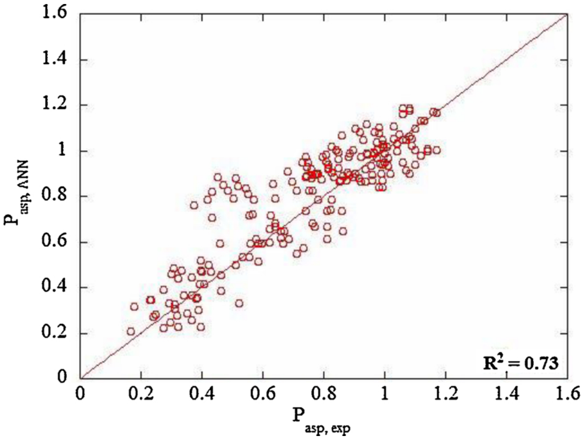

Fig. 7. Regression analysis for the ANN predictions of absolute aspiration pressure (P_{asp}) with respect to the experimental data.

overfitting issue is always raised when number of data points per parameter is small. In our study, the number was about 3.6 points per parameter even for the entire dataset. This is why we had to treat the data as a whole, leading the ANN to find a suboptimal result though is not perfect.

To validate the model equation further in terms of P_{asp}, we considered an extra experimental dataset for an annular slit convergent CCA nozzle [19]. Although this data had never been used in the foregoing ANN process (the training, validation, and test steps), Fig. 8 may correspond to the best example. On average, we would like to conclude that our model equation can make a reasonable prediction of aspiration pressure regardless of nozzle types, and relatively well reproduce the trend of the pressure as long as design and operation parameters lie in the ranges specified in Table 1. It is anticipated that the prediction accuracy of the model will increase as more data are accumulated, or we will be able to provide two sets of model equations for each type of CCA nozzles.

4. Sensitivity analysis of the dimensionless parameters and design guidelines for nozzles

While the present model equation is easy to use for a priori prediction of aspiration pressure, as shown in Section 3, it is difficult to extract any functional relation of P_{asp} in relation to other systematic parameters because the multiple parameters in Eq. (4) are complexly interrelated. One might need to reduce the number of systematic parameters in order to gain an insight into stable operation of the nozzles without concern for the aspiration pressure. For this purpose, we attempted three distinct parametric studies for the three groups of subset data sampled as described in Section 2.2.

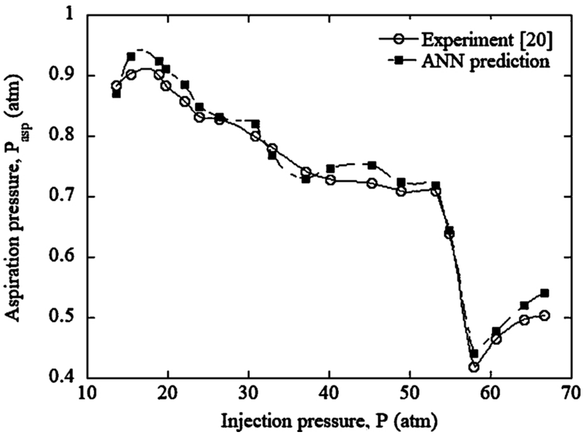

Fig. 8. Validation of the present model by experiment [20].

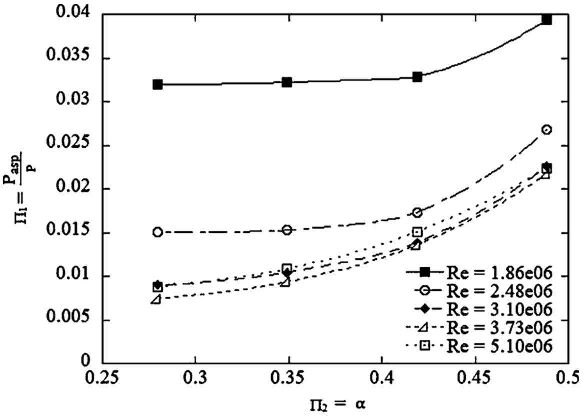

Fig. 9. Effect of the jet apex angle α on the dimensionless aspiration pressure Π_1.

First, we focused on the two apex angles Π_2 and Π_3 because these parameters are often reported as significant parameters, but conditionally [4,16]. A large apex angle is usually preferred for the production of smaller powders because it strengthens the gas-to-melt momentum transfer and decreases melt flow rates by increasing aspiration pressure, which turns out to be beneficial for producing finer powder [18]. However, too large apex angles sometimes increase the aspiration pressure so high that can eventually cause to block the melt flow [42]. This suggests that there exists a certain safe range of apex angles in view of stability within which the aspiration pressure buildup is suppressed and an optimal apex angle that might be the maximum value in the allowable range.

Based on the data in Tables B1 and B2 of Appendix B, we visualized the effect of the two apex angles (α and β) on the dimensionless aspiration pressure (Π_1) in Figs. 9 and 10, respectively. As a result, we observed that the aspiration pressure tends to increase exponentially with increase of the apex angle in both figures, when Re is larger than 3×10^6. It was also noted that the aspiration pressure does not vary significantly when α or $\beta \leq 0.4$ (22.5°) as if this apex angle is in the aforementioned safe range. Here, the angle of 22.5° seems to be the maximum allowable apex angle. Out of this range (see Table 1), both apex angles may make more significant influence on the aspiration pressure as consistent with literatures [4,16].

Table B3 and Fig. 11 show combined effects of tip protrusion length and Re as well as the kind of high-pressure gas used, respectively. For instance, the effect of apex angles again can be illustrated by the three symbols from the bottom of the figure legend (right triangle, filled

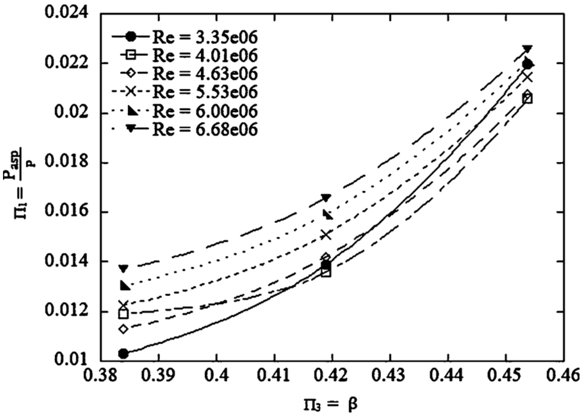

Fig. 10. Effect of the nozzle apex angle β on the dimensionless aspiration pressure Π_1.

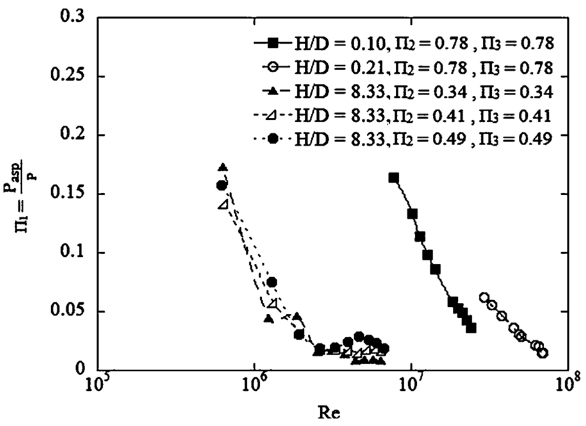

Fig. 11. Effects of *Re* number and apex angle on the dimensionless aspiration pressure Π_1.

circle, and triangle), whereas the effect of H/D is presented by the top two symbols (square and hollow circle). As for the apex angles, the figure shows that the Π_1 seems to be determined solely by *Re* number while the angle varies from 0.34 to 0.49 (around 22.5°), suggesting that the apex angles do not make a remarkable impact under this condition. On the other hand, when H/D increases at a fixed apex angle of ~45°, the two profiles denote a remarkable discrepancy. Thus, this seems to derive a conclusion that the protrusion length is a more influential parameter than the apex angle. However, we also have to say that this conclusion might be hasty because the dataset in Table B3 is not complete.

A sensitivity analysis using the elimination method [43] was conducted to allow quantitative evaluation of all the parameters and to extract the two most significant parameters. First, one parameter selected from among the four input parameters (Π_2, Π_3, Π_4, *Re*) was eliminated, and then the ANN process was performed on the remaining parameters to obtain a new model equation. Its prediction performance was compared with the original model obtained with all the input parameters, in terms of the coefficient of determination (R^2) and mean square error (MSE). If the eliminated parameter is critical to the determination of the aspiration pressure, the resulting new model will yield a relatively larger mean square error (MSE) and a smaller R^2 score due to the absence of the parameter.

Table 2 summarizes the results of this sensitivity analysis. Compared to the apex angles (Π_2 and Π_3), both Π_4 ($= H/D$) and *Re*, when eliminated, obviously brought about more significant degradation of the prediction performance of the model equation. It is thus concluded that the apex angles are relatively not significant parameters on aspiration pressure, as compared with Π_4 and *Re*.

For better understanding of the strong dependency of aspiration pressure on Π_4 and *Re*, CFD simulations were conducted. We considered two extreme cases of Π_4 (0.74 vs 10.04) at two different values of *Re* (6.81×10^5 and 2.33×10^7) while the apex angles remained constant at 0.7 (~40°). In Fig. 12, the velocity vectors were plotted with different colors corresponding to pressures in the range 0.074 − 2 atm. The CFD simulation results clearly demonstrated that the factors *H/D* and *Re* significantly alter the flow patterns and local pressure distributions around the tip of the melt tube.

Table 2
Sensitivity analysis for dimensionless aspiration pressure.

No.	Model	Eliminated input parameter	R^2	MSE
1.	Model 1	N/A	0.98	1.48×10^{-3}
2.	Model 2	Π3	0.92	3.04×10^{-3}
3.	Model 3	Π_3	0.90	8.88×10^{-3}
4.	Model 4	Π_4	0.82	2.23×10^{-2}
5.	Model 5	*Re*	0.078	1.18×10^{-1}

Fig. 12a shows that, for a short melt tube with small *H/D* of 0.74, after the main stream of gas is detached from the side wall of the melt tube, it forms a relatively short recirculation zone at a small *Re* of 6.81×10^5. When *Re* is increased to 2.33×10^7 by increasing the gas injection pressure *P*, the recirculation zone elongates to form an hourglass shape with an open end, consistent with the Schlieren imaging results [18]. This suggests that this case remains an open-wake condition in which the P_{asp} responds "in inverse proportion" to *P* (recall the observation of Ting et al. [1] in Introduction and the behavior in Fig. 3). This also explains why P_{asp} decreases from 1.13 atm to 0.35 atm with increase in *Re* or *P*. It is notable that the gas flow inside the recirculation zone seems to straighten directionally toward downstream at high *Re*, which limits the amount of gas returning to the melt tube tip, and decreases the P_{asp}.

Fig. 12b shows the flow fields at low and high *Re* numbers for a long melt tube of $H/D = 10.06$. The gas flow seems to be stronger compared to the case of a short melt tube, as if the gas flow is guided by the longer side-wall of the melt tube. At a low *Re* number, the main gas stream exhibits a more obvious pulsating pattern along the melt tube, resulting in a bit higher aspiration pressure of 1.29 atm. At a high *Re* number, the gas expands more directionally with the guidance of the melt tube so that it forms a stronger, muscle-like flow structure surrounding the melt tube. One might notice that at the tiny tip of the melt tube is created a very small (primary) recirculation zone ending in a Mach disk. Even though a secondary recirculation zone developed downstream of the Mach disk, it hardly affected the upstream pressure P_{asp} at the tip of the melt tube due to the resistance of the Mach disk. This resulted in a low aspiration pressure of 0.29 atm.

Finally, we attempted to create a guideline for the design and operation of annular plug nozzles without concern for the aspiration pressure. Recalling the conclusion of the sensitivity test, a contour map of P_{asp} was plotted against Π_4 and *Re* with a fixed apex angle (α and β) at 22.5°, as seen in Fig. 13. The red and dark-blue regions in the figure represent the maximum and minimum values of P_{asp}, respectively. As described in Introduction, there has been two competing aspects of aspiration pressure. Nevertheless, it should be noted that this guideline was made to direct toward lowering the aspiration pressure and could be differed if high apex angles are taken into account.

In Fig. 13, the over- and sub-ambient regions are separated with a dotted line. In other words, the dark blue region outside the dotted quadrant represents a sub-ambient pressure zone for $P_{asp} < 1$ atm, whereas it is advised that the conditions represented by the inside of the quadrant should be avoided. It is graphically obvious that any value of protrusion length (*H*) can be used when $Re > 10^6$; however, CCA nozzles with a long melt tube should be used with care under low-*Re* conditions. Particularly when $Re < 10^6$, a relatively short melt tube such as $H/D < 7$ is recommended to handle the stability issue, as indicated by a horizontal arrow in the figure. Similarly, if a long melt-tube nozzle must be used, higher-*Re* operation of the nozzle should be taken into account (see the vertical arrow).

While the contour map offers conceptual insight for reliable design and operation of close-coupled nozzles, the result should be used for nozzles with a fixed apex angle of 22.5°. However, we would like to note that the applicability of Fig. 13 can be readily extended by repeating the calculation of Eq. (4) for another apex angle. It should also be noted that operation expenses need to be considered in connection with performance, such as the preferred size and uniformity of the powder particles, prior to selecting optimal values for *Re* and *H/D*.

5. Conclusions

In this study, we developed an ANN-based methodology for a priori prediction of the aspiration pressure of close-coupled HPGA nozzles. The largest size of experimental data (206 in total) was used for the training, validating, and testing steps of the ANN. Based on the

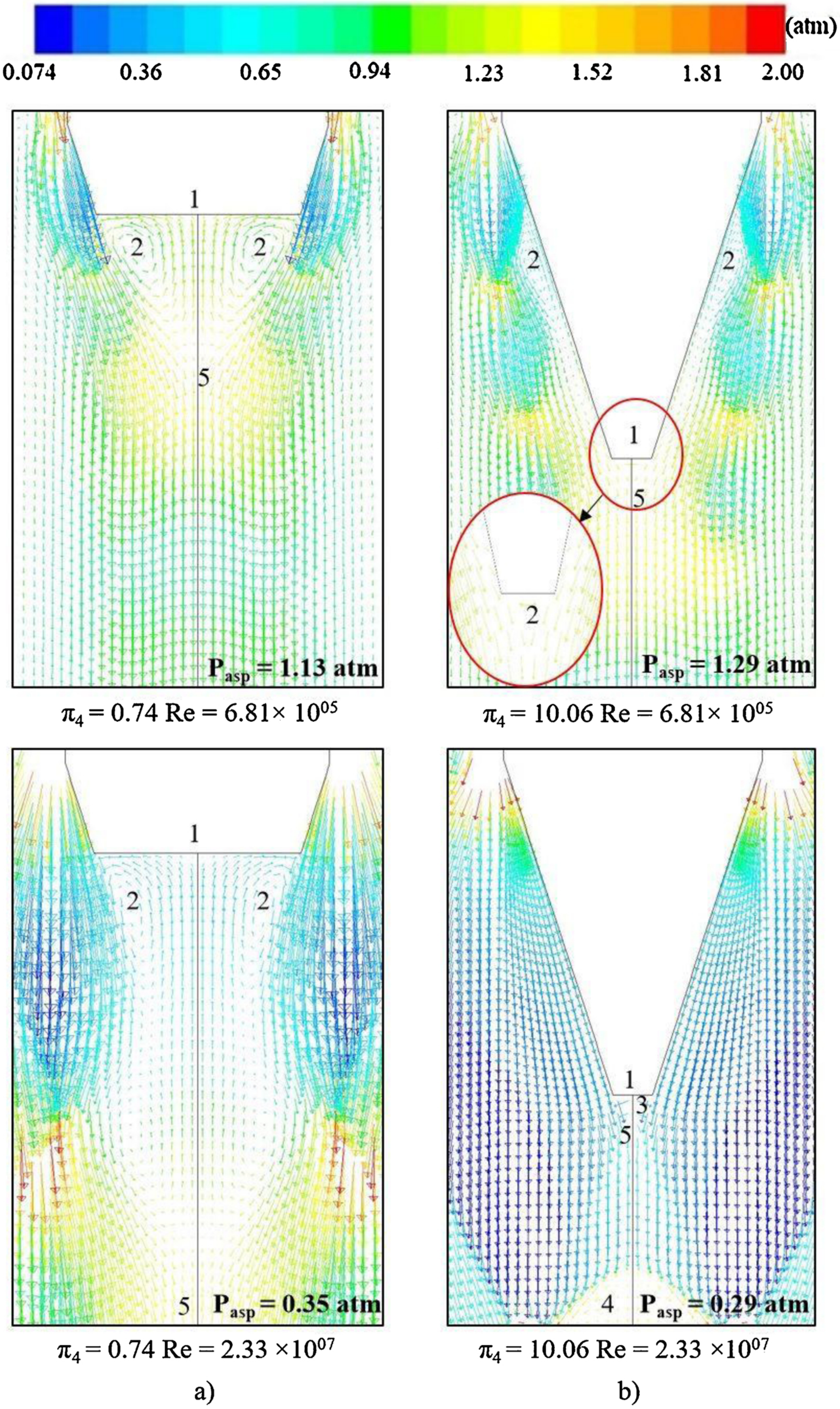

1 = Melt tube tip 2 = Recirculation zone
3 = Primary recirculation zone 4 = Secondary recirculation zone
5 = Stagnation front

Fig. 12. Vector plot of gas velocity overlaid with a pressure contour for a) $\Pi_4 = 0.74$ and $Re = 6.81 \times 10^5$ and 2.33×10^7, b) $\Pi_4 = 10.06$ and $Re = 6.81 \times 10^5$ and $2.33 \times 10^{7\cdot}$

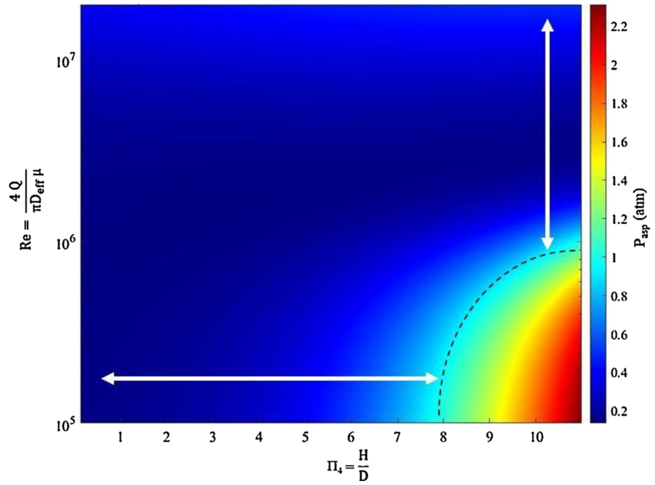

Fig. 13. Contour plot of P_{asp} as a function of Π_4 and *Re*.

preliminary tests, the present ANN was designed to include one input, one output, and one hidden layers. The LM back-propagation algorithm was finally employed for best training of the ANN. As a result, we obtained a new analytical model equation in a dimensionless form which is capable of nicely predicting the aspiration pressure over a wide range of gas and nozzle-design parameters, with a high coefficient of determination of $R^2 = 0.98$ and a low MSE of 1.48×10^{-3}. However, the prediction accuracy for absolute aspiration pressures becomes considerably degraded with a decrease of R^2 score to 0.73 and an average relative prediction error of 17 %. The model equation was further validated using an experimental dataset that had never been used in any of the previous steps. A sensitivity test was performed and revealed that *H/D* and *Re* are apparently more significant than the apex angles. Finally, a contour map of the aspiration pressure prepared as a function of *H/D* and *Re* suggested that any protrusion length of melt tubes can be used at high *Re* numbers while short melt tubes are recommended for lowering the aspiration pressure in case of low apex angles. However, this result should be accepted to have clear limitations arising from insufficient size of literature data.

Declaration of Competing Interest

The authors declare that they have no known competing financial interests or personal relationships that could have appeared to influence the work reported in this paper.

Acknowledgements

This work was supported by the National Research Foundation of Korea for research number of No. 2019R1I1A3A01063854 and also by Samsung Electronics DS Industry-University Cooperation Center.

Appendix A. Details of set-up parameters for running ANN

where mu is the control parameter for the algorithm used to train the neural network.

ANN training parameters	
Maximum number of epochs to train	5000
Maximum validation failures	20
Learning rate	0.01
Performance goal	0.00
Minimum gradient	1×10^{-10}
Initial mu (damping factor)	1
mu decrease factor	0.8
mu increase factor	1.5

Appendix B. Sub-data groups for parametric studies

Table B1
The first data group of dimensionless parameters sampled from literature datasets aiming at parametric study for the effect of the gas apex α.

Re	Π_2	Π_3	Π_4	Π_1	*Re*	Π_2	Π_3	Π_4	Π_1
1.87E+06	0.28	0.28	0.83	3.43E-01	2.48E+06	0.28	0.28	0.83	2.63E-02
	0.35	0.35	0.83	4.65E-01		0.35	0.35	0.83	1.56E-02
	0.42	0.42	0.83	3.14E-01		0.42	0.42	0.83	1.79E-02
	0.49	0.49	0.83	3.10E-01		0.49	0.49	0.83	1.90E-02
3.10E+06	0.28	0.28	0.83	8.88E-03	3.73E+06	0.28	0.28	0.83	1.20E-02
	0.35	0.35	0.83	1.67E-02		0.35	0.35	0.83	1.36E-02
	0.42	0.42	0.83	1.80E-02		0.42	0.42	0.83	1.68E-02
	0.49	0.49	0.83	1.98E-02		0.49	0.49	0.83	2.43E-02
5.00E+06	0.28	0.28	0.83	8.17E-03					
	0.35	0.35	0.83	8.97E-03					
	0.42	0.42	0.83	1.72E-02					
	0.49	0.49	0.83	2.64E-02					

Table B2
The second data group of dimensionless parameters sampled from literature datasets aiming at parametric study for the effect of the gas apex β.

Re	Π_2	Π_3	Π_4	Π_1	Re	Π_2	Π_3	Π_4	Π_1
3.35E+06	0.42	0.39	3.80	1.46E-02	5.33E+06	0.42	0.39	3.56	1.01E-02
	0.42	0.42	3.80	1.68E-02		0.42	0.42	3.56	1.30E-02
	0.42	0.51	3.80	2.42E-02		0.42	0.51	3.56	2.25E-02
4.01E+06	0.42	0.39	3.67	1.21E-02	6.00E+06	0.42	0.39	3.47	8.40E-03
	0.42	0.42	3.67	1.47E-02		0.42	0.42	3.47	1.16E-02
	0.42	0.51	3.67	2.31E-02		0.42	0.51	3.47	2.22E-02
4.63E+06	0.42	0.39	3.67	1.21E-02	6.68E+06	0.42	0.39	3.47	8.40E-03
	0.42	0.42	3.67	1.47E-02		0.42	0.42	3.47	1.16E-02
	0.42	0.51	3.67	2.31E-02		0.42	0.51	3.47	2.22E-02

Table B3
The third data group of dimensionless parameters sampled from literature datasets aiming at parametric study for the effects of the protrusion length of nozzle $\Pi_4 = H/D$ and Re number.

Π_2	Π_3	Π_4	Re	Π_1	Π_2	Π_3	Π_4	Re	Π_1
0.79	0.79	0.10	7.70E+06	1.64E-01	0.34	0.34	8.33	6.27E+05	1.73E-01
0.79	0.79	0.10	1.02E+07	1.34E-01	0.34	0.34	8.33	1.24E+06	4.43E-02
0.79	0.79	0.10	1.13E+07	1.14E-01	0.34	0.34	8.33	1.85E+06	4.65E-02
0.79	0.79	0.10	1.28E+07	9.81E-02	0.34	0.34	8.33	2.53E+06	1.56E-02
0.79	0.79	0.10	1.41E+07	8.64E-02	0.34	0.34	8.33	3.13E+06	1.67E-02
0.79	0.79	0.10	1.84E+07	5.86E-02	0.34	0.34	8.33	3.76E+06	1.36E-02
0.79	0.79	0.10	1.98E+07	5.30E-02	0.34	0.34	8.33	4.39E+06	8.81E-03
0.79	0.79	0.10	2.12E+07	4.87E-02	0.34	0.34	8.33	5.06E+06	8.97E-03
0.79	0.79	0.10	2.27E+07	4.28E-02	0.34	0.34	8.33	5.70E+06	9.38E-03
0.79	0.79	0.10	2.41E+07	3.66E-02	0.34	0.34	8.33	6.36E+06	8.00E-03
0.79	0.79	0.21	2.93E+07	6.19E-02	0.41	0.41	8.33	6.48E+05	1.42E-01
0.79	0.79	0.21	3.27E+07	5.52E-02	0.41	0.41	8.33	1.33E+06	5.72E-02
0.79	0.79	0.21	3.80E+07	4.67E-02	0.41	0.41	8.33	1.99E+06	3.14E-02
0.79	0.79	0.21	4.51E+07	3.59E-02	0.41	0.41	8.33	2.68E+06	1.79E-02
0.79	0.79	0.21	4.88E+07	3.08E-02	0.41	0.41	8.33	3.36E+06	1.80E-02
0.79	0.79	0.21	5.01E+07	2.90E-02	0.41	0.41	8.33	4.01E+06	1.68E-02
0.79	0.79	0.21	6.16E+07	2.17E-02	0.41	0.41	8.33	4.62E+06	1.53E-02
0.79	0.79	0.21	6.47E+07	2.01E-02	0.41	0.41	8.33	5.32E+06	1.72E-02
0.79	0.79	0.21	6.81E+07	1.52E-02	0.41	0.41	8.33	5.97E+06	1.84E-02
0.79	0.79	0.21	6.90E+07	1.52E-02	0.41	0.41	8.33	6.58E+06	1.66E-02
0.43	0.43	5.00	3.47E+05	1.01E-01	0.49	0.49	8.33	6.22E+05	1.58E-01
0.43	0.43	5.00	5.01E+05	6.80E-02	0.49	0.49	8.33	1.29E+06	7.51E-02
0.43	0.43	5.00	6.43E+05	5.06E-02	0.49	0.49	8.33	1.94E+06	3.10E-02
0.43	0.43	5.00	8.95E+05	4.02E-02	0.49	0.49	8.33	2.61E+06	1.90E-02
0.43	0.43	5.00	1.15E+06	2.82E-02	0.49	0.49	8.33	3.29E+06	1.98E-02
					0.49	0.49	8.33	3,988,900	2.43E-02
					0.49	0.49	8.33	4,650,600	2.88E-02
					0.49	0.49	8.33	5,350,300	2.64E-02
					0.49	0.49	8.33	5,966,200	2.28E-02

Appendix C. Aspiration pressure prediction equation by ANN

1. *st step: Normalization of inputs and outputs*

Before the training process, both the inputs and outputs were normalized in the range [-1,1] by Eq. 3.

2. *nd step: Training of the ANN to obtain the best set of weights and biases*

After successful training, MATLAB provided the set of weights and biases for the best prediction of output signal. The best result was summarized in the table below. Recall that the two indices, *i* and *j*, indicate the *i*th input and *j*th hidden neuron as illustrated in Fig. 1. Thus, the weight w_{ij} could be said to evaluate the significance of the *i*–*j* connection.

w_{ij}					c_j	$w_{jk,\ k=1}$	$d_{k,\ k=1}$
i / j	1	2	3	4			
1	0.126	-0.166	0.042	0.006	-1.387	-6.070	4.962
2	-1.336	1.151	0.303	-22.481	-24.237	8.453	
3	4.215	-3.907	-0.677	3.700	0.574	-11.687	
4	-3.421	-0.176	-0.054	0.015	2.605	-14.46	

3. rd step: Calculation of the activations and sigmoid functions

Based on the result of the table above, four activations (a_j) were calculated from the four input neurons with the weights w_{ij} and biases c_j. Next step is to sequentially calculate the sigmoid functions (z_j). Refer to Section 2.2 for the mathematical expressions of the activation and sigmoid function.

4. th step: Calculation of output signal

The last equation representing the normalized output signal was expressed as:

$$\bar{\Pi}_1 = -12.14/(1 + \exp(-2a_1)) + 16.906/(1 + \exp(-2a_1)) - 23.374/(1 + \exp(-2a_1)) - 28.922/1 + \exp(-2a_1) + 28.727$$

5. th step: De-normalization of the output signal and the final equation for prediction of P_{asp}

At the 5th step, the normalized output $\bar{\Pi}_1$ was denormalized inversely using Eq. 3 as:

$$o_k = (o_{max} - o_{min}) \times (\bar{\Pi}_1 + 1)/2 + o_{min}$$

$$= 5.656 - 2.306/(1 + \exp(-2a_1)) + 3.212/(1 + \exp(-2a_2)) - 4.441/(1 + \exp(-2a_3)) - 5.495/(1 + \exp(-2a_4))$$

where $o_{max} = 0.39$ and $o_{min} = 5.2 \times 10^{-3}$. This dimensionless form of equation was sequentially converted to the final equation (Eq. 4) for prediction of aspiration pressure.

Appendix D. Supplementary data

Supplementary material related to this article can be found, in the online version, at doi:https://doi.org/10.1016/j.cep.2020.107924.

References

[1] J. Ting, M.W. Peretti, W.B. Eisen, The effect of wake-closure phenomenon on gas atomization performance, Mater. Sci. Eng., A 326 (1) (2002) 110–121.

[2] S. Sarkar, W. Prashanth, T. Anand, P. Sivaprasad, S. Bakshi, Study of primary breakup of molten tin during powder production in free-fall configuration, At. Sprays 27 (3) (2017) 269–284.

[3] P. Shukla, R. Mandal, S. Ojha, Non-equilibrium solidification of undercooled droplets during atomization process, Bull. Mater. Sci. 24 (5) (2001) 547–554.

[4] C. Cui, F. Cao, Q. Li, Formation mechanism of the pressure zone at the tip of the melt delivery tube during the spray forming process, J. Mater. Process. Technol. 137 (1) (2003) 5–9.

[5] H. Liu, E. Lavernia, R. Rangel, An analysis of freeze-up phenomena during gas atomization of metals, Int. J. Heat Mass Transf. - Theory Appl. 38 (12) (1995) 2183–2193.

[6] M. Jeyakumar, S. Kumar, G. Gupta, The influence of processing parameters on characteristics of an aluminum alloy spray deposition, Mater. Manuf. Process. 24 (6) (2009) 693–699.

[7] J. Baram, Pressure characteristics at the pour-tube orifice in ultrasonic gas atomization, Mater. Sci. Eng. 98 (1988) 65–69.

[8] D.R. Glass, Effects of acoustic feedback on the spread and decay of supersonic jets, AIAA Journal 6 (10) (1968) 1890–1897.

[9] R. Ünal, The influence of the pressure formation at the tip of the melt delivery tube on tin powder size and gas/melt ratio in gas atomization method, J. Mater. Process. Technol. 180 (1) (2006) 291–295.

[10] R. Unal, Investigation on metal powder production efficiency of new convergent divergent nozzle in close coupled gas atomisation, Powder Metall. 50 (4) (2007) 302–306.

[11] A. Aksoy, R. Unal, Effects of gas pressure and protrusion length of melt delivery tube on powder size and powder morphology of nitrogen gas atomised tin powders, Powder Metall. 49 (4) (2006) 349–354.

[12] O. Aydin, R. Unal, Experimental and numerical modeling of the gas atomization nozzle for gas flow behavior, Comput. Fluids 42 (1) (2011) 37–43.

[13] J. Meyer, Advanced gas atomization production of oxide dispersion strengthened (ODS) Ni-base superalloys through process and solidification control", Graduate Theses and Dissertations, Iowa State Univ. Vet. (2013).

[14] J. Mi, R.S. Figliola, I.E. Anderson, A numerical investigation of gas flow effects on high-pressure gas atomization due to melt tip geometry variation, Metall. Mat. Trans. B 28 (5) (1997) 935–941.

[15] S. Motaman, A.M. Mullis, R.F. Cochrane, D.J. Borman, Numerical and experimental investigations of the effect of melt delivery nozzle design on the open-to closed-wake transition in closed-coupled gas atomization, Metall. Mater. Trans. B 46 (4) (2015) 1990–2004.

[16] X.M. Zhao, J. Xu, X.X. Zhu, S.M. Zhang, Variation mechanism of aspiration pressure at the tip of metal delivery tube in supersonic atomization, Mater. Sci. Forum, Trans Tech Publications 675 (2011) 1049–1052.

[17] V. Srivastava, S. Ojha, Effect of aspiration and gas-melt configuration in close coupled nozzle on powder productivity, Powder Metall. 49 (3) (2013) 213–218.

[18] S.P. Mates, G.S. Settles, A study of liquid metal atomization using close-coupled nozzles, Part 1: gas dynamic behavior, At. Sprays 15 (1) (2005) 19–40.

[19] D. Schwenck, N. Ellendt, J. Fischer-Bühner, P. Hofmann, V. Uhlenwinkel, A novel convergent-divergent annular nozzle design for close-coupled atomisation, Powder Metall. 60 (3) (2017) 198–207.

[20] J. Ting, I.E. Anderson, A computational fluid dynamics (CFD) investigation of the wake closure phenomenon, Mater. Sci. Eng., A 379 (1) (2004) 264–276.

[21] S. Ridder, S. Oscella, P. Espina, F. Biancaniello, Intelligent control of particle size distribution during gas atomization, Int. J. Powder Met. 28 (2) (1992) 133–147.

[22] E. Buckingham, On physically similar systems; illustrations of the use of dimensional equations, Phys. Rev. 4 (4) (1914) 345–376.

[23] P. Modi, S. Seth, Hydraulics and Fluid Mechanics: Including Hydraulic Machines (in SI Units), Standard Book House, Delhi, India, 2011.

[24] G. Liu, L. Jia, B. Kong, S. Feng, H. Zhang, H. Zhang, Artificial neural network application to microstructure design of Nb-Si alloy to improve ultimate tensile strength, Mater. Sci. Eng., A 707 (2017) 452–458.

[25] T. Ghode, K.M.M.S. Begum, A.B. Desamala, A. Narayanan, A comparative study of ann and cfd modelling for pressure drop prediction in a fluidized bed with internals, Indian Chem. Eng. 59 (1) (2017) 57–75.

[26] A. Sharifi, A. Mohebbi, Introducing a new formula based on an artificial neural network for prediction of droplet size in venturi scrubbers, Braz. J. Chem. Eng. 29 (2012) 549–558.

[27] T. Al-Wahaibi, F.S. Mjalli, Chem. Eng. Commun. 201 (2) (2014) 209–224.

[28] T. Varol, A. Canakci, S. Ozsahin, Artificial neural network modeling to effect reinforcement properties on the physical and mechanical properties of Al2024–B4C composites produced by powder metallurgy, Compos. Part B Eng. 54 (2013) 224–233.

[29] Y.K. Mohanty, B.P. Mohanty, G.K. Roy, K.C. Biswal, Effect of secondary fluidizing medium on hydrodynamics of gas-solid fluidized bed—statistical and ANN approaches, Chem. Eng. J. 148 (1) (2009) 41–49.

[30] M. Pradhan, R. Das, C. Biswas, Comparisons of neural network models on surface roughness in electrical discharge machining, Proceedings of the institution of mechanical engineers, part B, J. Eng. Manuf. 223 (7) (2009) 801–808.

[31] S. Haykin, Neural Networks: A Comprehensive Foundation, 2nd edition, Macmillan, New York, 1998.

[32] G.E. Hinton, How neural networks learn from experience, Sci. Am. 267 (3) (1992) 144–151.

[33] MATLAB And Deep Learning Toolbox Release, The MathWorks, Inc., Natick, Massachusetts, United States, 2018.

[34] K. Hornik, M. Stinchcombe, H. White, Multilayer feedforward networks are universal approximators, Neural Netw. 2 (5) (1989) 359–366.

[35] J.G. Rueckl, K.R. Cave, S.M. Kosslyn, Why are "what" and "where" processed by separate cortical visual systems? A computational investigation, J. Cognit. Neurosci. 1 (2) (1989) 171–186.

[36] K. Shahbaz, S. Baroutian, F. Mjalli, M. Hashim, I. AlNashef, Densities of ammonium and phosphonium based deep eutectic solvents: prediction using artificial intelligence and group contribution techniques, Thermochim. Acta 527 (2012) 59–66.

[37] A. Blum, Neural Networks in C+ +: an Object-oriented Framework for Building Connectionist Systems, John Wiley & Sons, New York, 1992.

[38] M.J. Berry, G.S. Linoff, Data Mining Techniques: for Marketing, Sales, and Customer

Relationship Management, John Wiley & Sons, New York, 2004.

[39] M. Qiu, Y. Song, F. Akagi, Application of artificial neural network for the prediction of stock market returns: the case of the Japanese stock market, Chaos, Solitons Fractals 85 (2016) 1–7.

[40] R. Kaiser, C. Li, S. Yang, D. Lee, A numerical simulation study of the path-resolved breakup behaviors of molten metal in high-pressure gas atomization: with emphasis on the role of shock waves in the gas/molten metal interaction, Adv. Powder Technol. 29 (3) (2018) 623–630.

[41] D.A. Firmansyah, R. Kaiser, R. Zahaf, Z. Coker, T.Y. Choi, D. Lee, Numerical simulations of supersonic gas atomization of liquid metal droplets, Jpn. J. Appl. Phys. 53 (5S3) (2014) 05HA09.

[42] I.E. Anderson, R.L. Terpstra, R. Figliola, Analysis of gas recirculation flow effects in the melt feeding zone of a close-coupled gas atomization nozzle, Powder Materials: Current Research and Industrial Practices III, (2010), pp. 1–20.

[43] S. Lek, A. Belaud, P. Baran, I. Dimopoulos, M. Delacoste, Role of some environmental variables in trout abundance models using neural networks, Aquat. Living Resour. 9 (1) (1996) 23–29.